# An image processing approach to reconstruct wind using long-range wind lidars

**M Nafisifard**[1,*][0000−0001−7494−4985], **J B Jakobsen**[1][0000−0001−9548−026X], **J T Snæbjörnsson**[1,2][0000−0003−4391−9925], **H Ágústsson**[3], **M S Grønsleth**[3], and **O Undheim**[3,4]

[1]Department of Mechanical and Structural Engineering and Material Science, University of Stavanger, Kjell Arholmsgate 41, Stavanger, Norway.
[2]Department of Engineering, Reykjavik University, Menntavegur 1 IS-101, Reykjavík, Iceland.
[3]Kjeller Vindteknikk, Norconsult Group, Norway
[4]Statkraft, Norway.

E-mail: *mohammad.nafisifard@uis.no

**Abstract.** Lidar-based wind sensing technology, originally used in the wind energy sector, is now being utilized in wind engineering to monitor wind action for designing fjord-crossing infrastructure like long-span bridges. Accurate estimation of design wind loads is crucial for the design process of such bridges. This paper examines wind data from two pairs of long-range lidars positioned along one side of the Sulafjorden, Norway, in a measurement campaign initiated by the Norwegian Public Roads Administration (NPRA). Two different scanning modes, the Plan Position Indicator (PPI) mode and the staring mode, with the fixed line-of-sight (LOS) orientation, are used to determine the line-of-sight wind speeds, the wind direction, and the related along wind speed. An image processing approach is used to compute along wind velocity information from all range gates based on the LOS wind speeds from two near-parallel lidar beams. The estimated along wind velocity is validated through wind data calculated at the intersection point of the two lidars, which provides velocity data with two horizontal components. The image-based reconstruction is found to produce reasonable wind speed estimates with a goodness-of-fit coefficient of $R^2 = 0.903$. The mean wind direction estimate is smoothened but still comparable to the actual wind direction. The image processing approach shows promising potential to provide wind speed and direction information for all range gates for the lidar setup used, which can supplement traditional single-point wind velocity characterization by dual lidars.

## 1. Introduction

The construction of long-span bridges across wide and deep fjords presents challenging design tasks. Accurate estimation of design wind loads is crucial in the design process, and this requires a thorough understanding of the local wind patterns. Fortunately, advancements in optical remote wind sensing instruments, such as Doppler wind lidars, have made it possible to gain valuable insights into wind patterns in hard-to-reach areas, supplementing conventional mast-based anemometry. Short-range Doppler lidars, capable of measuring winds within a few hundred meters, have been used to map turbulent flow around a suspension bridge [1, 2, 3]. Long-range wind lidars have also been used to access wind conditions relevant to fjord crossings. In 2014, Cheynet et al. [4] conducted a lidar measurement campaign, employing a long-range scanning pulsed coherent lidar positioned 1.75 km to the west of the Lysefjord Bridge. The outcomes of the

analysis revealed that lidars have the potential to complement anemometers in the examination of wind effects on large, wind-sensitive structures. In 2017, Cheynet et al. [5] assessed the measurements of three synchronized long-range pulsed wind lidars at a planned bridge site in terms of wind spectrum for the along-wind component and lateral wind co-coherence. Using single pulsed Doppler wind lidar, Cheynet et al. [6] achieved coherence estimates in overall good agreements with IEC and Frøya coherence models [7, 8] from the PPI and the Range Height Indicator (RHI) scan for cross-flow separation from 20 m to 85 m.

In a recent investigation initiated by the NPRA and carried out by the Kjeller Vindteknikk from the Norconsult Group in Norway [9, 10], four long-range Doppler lidars, organized into two pairs, were used to map wind conditions in the Sulafjorden in Western Norway at a designated bridge location. The remote wind observations complement the key data acquired by the sonic anemometers on tall masts. The overall measurement campaign and the related numerical simulations are described in [11]. The resulting wind data plays a pivotal role in understanding the anticipated wind-related loads that will impact the proposed bridge crossing the fjord e.g. [12].

The proof-of-concept study presented in this paper utilizes data from [10]. An image processing approach is deployed to construct the along wind velocity and direction for any desired distance between the lidar and measurement point (also called the range gate centre) along a lidar beam with a fixed orientation, based on the relative comparison with nearly-parallel lidar beams. This approach is complementary and/or alternative approach to the traditional evaluation of 2D horizontal velocity components based on two crossing lidar beams. The approach adopted is based on an image processing technique [13] successfully applied in other fields of science [14].

The paper is organized into several sections. Section 2 provides an overview of the measurement site, including essential details about Sulafjorden and the instrumentation. Section 3 explains the setup of the lidar measurements and the image processing approach used to analyze wind data. Section 4 presents a comprehensive account of wind field characterization using PPI scanning mode within the fjord, along with the temporal evolution of wind direction and velocity fluctuations near the centre of the intended bridge location. Finally, Section 5 concludes the study and provides recommendations for future research.

## 2. Measurement Site and Monitoring System

Sulafjorden is situated around 10 km southwest of Ålesund. It is a fjord that divides the municipalities of Hareid on the Hareidlandet in the west and Sula in the east (see fig. 1-bottom right). The fjord runs along a south-southeast north-northwest axis and is approximately 12 km long, 3.1 km wide, and has a depth of 300 m. The mountain slopes above the fjord are steep and reach heights of 500 - 600 m above sea level at the bridge-shore connections.

The lidar measurement system consists of 4 scanning lidars, Windcube 400S [15], which are located on the west side of the fjord. Two of these lidars, Dolly and Minni, are situated at Kvitneset, the western end of the planned bridge. The other two lidars, Donald and Mikke, are located further south at Saudebøen, near Brandal. Since the lidars at Kvitneset are near the end of the planned bridge, one of the lidar beams can measure along the bridge span and form lidar pairs with both lidars at Saudebøen. This setup allows three lidars to measure the vector wind in two locations simultaneously, while the fourth lidar can perform independent descriptive scans. All lidars are positioned at an elevation similar to the height of the planned bridge deck at the fjord centre, 80 m above sea level, enabling the lidar beams to remain close to horizontal.

Two distinct scanning modes were employed: PPI (Plan Position Indicator) and LOS (sequential fixed Line-of-Sight measurement). The WINDCUBE 400S concurrently records wind velocities at multiple positions along the scanning beam. When considering an azimuth angle $\phi$, an elevation angle $\theta$, and a radial distance $r$, the lidar is specifically designed to measure the wind velocity component along the beam's trajectory at specific ranges. In this paper, the

**Figure 1.** Long-range lidars at Kvitneset (top) at Saudebøen (bottom-left) the map from www.norgeskart.net (bottom-right), and lidar positions indicated by green dots on.

azimuth angle is defined as the angle between the projection of the line of sight on the local horizontal plane and the geometric North (varies between 0° and 360°), while the elevation angle is defined as the angle between the line of sight and the local horizontal plane (varies between -90° and 90°). The PPI and LOS scanning modes can be characterized solely by using the azimuth and elevation angles. The PPI scan involves scanning at a consistent elevation while varying azimuth angles, whereas the LOS scan maintains a fixed azimuth and elevation angle. For LOS modes of operation with the WindScanner software, two or more lidars have operated in a synchronized fashion, that is, the master software has ensured that each sampling is done synchronously with a time difference of 50 ms or less. In the LOS mode, the data are sampled at a rate of 1 Hz. In the PPI mode, each 1.5° sector is revisited once every 145 seconds. The key parameters of the scanning patterns are summarized in Table 1.

**Table 1.** Parameters used for each scanning scenario.

| Parameters | PPI | LOS | | |
| --- | --- | --- | --- | --- |
| | Minni | Donald | Mikke | Dolly |
| Azimuth (°) | -39 to 170 | 34.95 | 36.08 | 76.67 |
| Elevation (°) | 0 | 0.44 | 0.28 | 0.76 |
| Sampling frequency (Hz) | 0.0069 | 1 | 1 | 1 |
| Scan speed (°/s) | 1.42 | - | - | - |
| Accumulation time (s) | 0.70 | 1 | 1 | 1 |
| Approximate duration (min) | 60 | 60 | 60 | 60 |
| Range gate length (m) | 75 | 75 | 75 | 75 |
| Range gate step (m) | 25 | 25 | 25 | 25 |
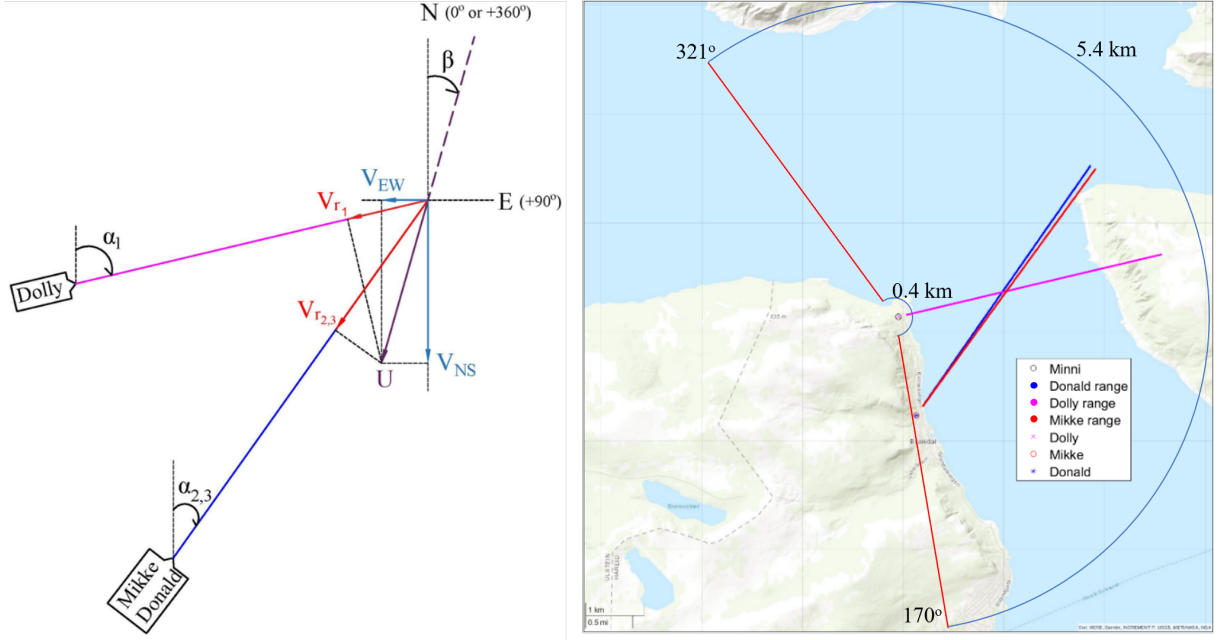


**Figure 2.** (left) Plan view of the measurement setup for LOS mode. (right) The measurement domain of the lidars.

## 3. Analysis Methods

### 3.1. Wind velocity direct formulation

Through the application of synchronized lidar-derived along-beam wind velocity data ($v_{r_1}$ and $v_{r_2}$), in a horizontal plane (see fig. 2-left), one can ascertain the wind components in any direction in the horizontal plane with the provision that the scanning beams intersect at large enough angles. Through the following mathematical transformations, the components along the geographic North-South and East-West ($v_{NS}$ and $v_{EW}$) are identified.

$$\begin{bmatrix} v_{EW} \\ v_{NS} \end{bmatrix} = \mathbf{M}^{-1} \begin{bmatrix} v_{r_1} \\ v_{r_{2,3}} \end{bmatrix} \tag{1}$$

where

$$\mathbf{M} = \begin{bmatrix} \sin{(\alpha_1)} & \cos{(\alpha_1)} \\ \sin{(\alpha_{2,3})} & \cos{(\alpha_{2,3})} \end{bmatrix} \tag{2}$$

The instantaneous horizontal wind data along the geographic North-South and East-West, can then be processed to retrieve the associated main wind direction and the along wind velocity, denoted by $\beta$ and $U$, respectively. To compute $\beta$ the following transformation is used.

$$\beta(t) = \arctan\left(\frac{v_{EW}(t)}{v_{NS}(t)}\right) \tag{3}$$

The wind velocity $U$ is computed as

$$U(t) = \sqrt{v_{EW}(t)^2 + v_{NS}(t)^2} \tag{4}$$

This information is only available at the two points where the lidar beams from Donald and Mikke cross the lidar beam from Dolly. Therefore to evaluate the wind direction and the along wind velocity for other locations along the scanning path of Donald and Mikke, another approach is required. It is the objective of this paper to demonstrate the possibility of using parametric image alignment for that purpose.

*3.2. Parametric Image Alignment*

The objective of image alignment is to quantify the distortion between one or multiple input images with regard to a reference image, so-called template image, aiming to minimize a measure of dissimilarity between the template and the warped images. When prior knowledge about the type of difference occurring between the template and input images is available, this problem is commonly termed parametric image alignment [16]. Parametric image alignment can be used for various purposes, with one example being template tracking such as Enhanced Correlation Coefficient Maximization (ECC) [13]. In template tracking tasks, the number of variables involved is typically limited, making it possible to achieve satisfactory results using a general-purpose optimization approach.

The alignment challenge consists of identifying the set of coordinates in the warped image $I_w(\mathbf{y})$, at which the image has the greatest similarity with the template image $I_r(\mathbf{x})$. The coordinates in the region of interest in the template image $\mathbf{x}_k$, $k = 1, ..., K$ are mapped onto the coordinates in the warped image using a warping transformation $\psi(\mathbf{x}; \mathbf{p})$, $\mathbf{y}_k(\mathbf{p}) = \psi(\mathbf{x}_k; \mathbf{p})$, $k = 1, ..., K$. The coordinates $\mathbf{x}_k$ and $\mathbf{y}_k$ are partly shown in fig. 5 (bottom) as the red dots which form the basis of wind mapping images. In the ECC technique, the reference vector $\mathbf{i}_r$ and the associated warped vector $\mathbf{i}_w(\mathbf{p})$ are defined as

$$\mathbf{i}_r = [I_r(\mathbf{x}_1) \quad I_r(\mathbf{x}_2) \quad \cdots \quad I_r(\mathbf{x}_k)]^t \tag{5}$$

$$\mathbf{i}_w(\mathbf{p}) = [I_w(\mathbf{y}_1(\mathbf{p})) \quad I_w(\mathbf{y}_2(\mathbf{p})) \quad \cdots \quad I_w(\mathbf{y}_k(\mathbf{p}))]^t \tag{6}$$

and the following criterion to quantify the performance of the warping transformation is proposed

$$E_{ECC}(\mathbf{p}) = \left\| \frac{\bar{\mathbf{i}}_r}{\|\bar{\mathbf{i}}_r\|} - \frac{\bar{\mathbf{i}}_w(\mathbf{p})}{\|\bar{\mathbf{i}}_w(\mathbf{p})\|} \right\|^2 \tag{7}$$

where $\|\cdot\|$ denotes the Euclidean norm and $\bar{X}$ is the averaging operator. The problem is to find $\mathbf{p}$ where $\mathbf{p} = [p_1, ..., p_N]^t$ is a vector of unknown parameters in such a way that $E_{ECC}(\mathbf{p})$ be minimized. With certain assumptions in place (like $N < K$), this problem can be solved using an iterative procedure. More details of the problem-solving process can be found in [13, 16].
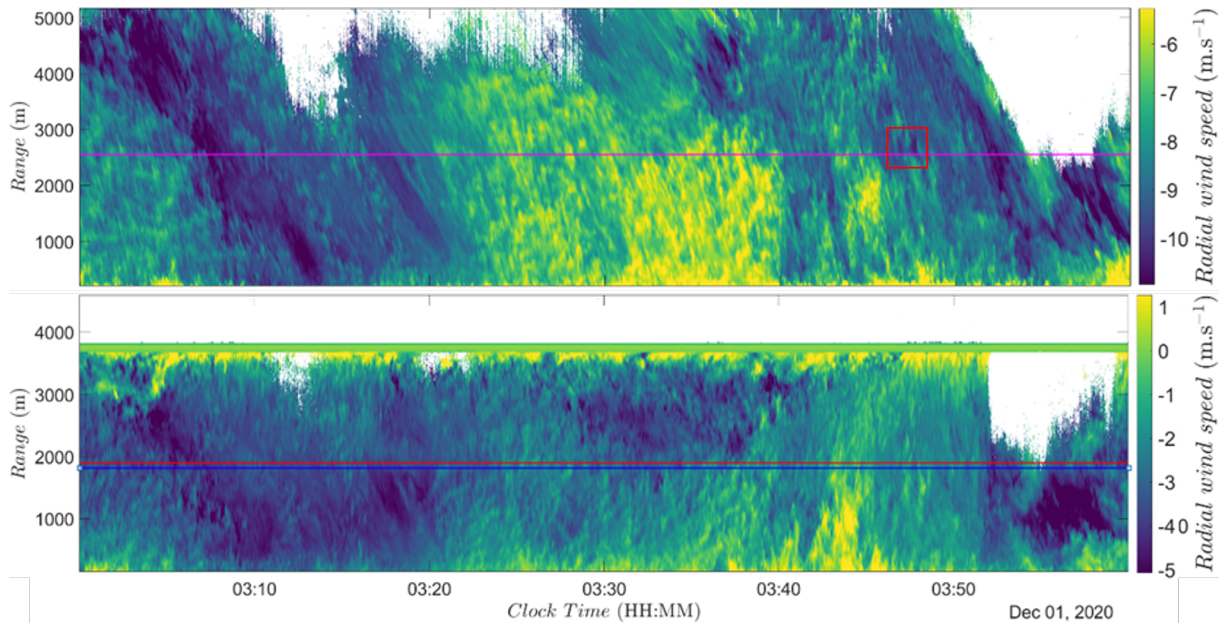
**Figure 3.** Spatiotemporal fluctuations of wind velocity recorded on 1 December 2020, 03:00 to 04:00 by (top) Donald and (bottom) Dolly. Intersection with other lidar(s) are indicated by colour horizontal lines.

### 3.3. Data availability

In order to measure the wind, a lidar depends on the existence of aerosols in the air that it probes. If there are no aerosols, there will be no measurements. If there are too many aerosols, for instance, heavy fog, the signal will be attenuated quickly, and the measurement range will be reduced. Therefore, the availability of lidar measurements varies with the atmospheric conditions.

The lidar internally calculates the Carrier-to-Noise Ratio (CNR) which is defined as the Signal-to-Noise Ratio (SNR) on each high-frequency sampling. This quantity depends on the aerosol concentration in the atmosphere. A high atmospheric backscatter coefficient leads to high CNR. CNR level depends on weather conditions. CNR can then be used in the filtering of the raw data. Good quality data typically has a CNR value in the range of -27 to 0 dB [17]. In this study, A constant threshold of -27 dB has been employed to define reliable data, which removes nearly all spurious data values. Subsequently, linear interpolation has been used to fill filtered data in the datasets recorded on December 2020, 03:00 to 04:00, at moderate wind speeds. The data is of good quality and used further in the image processing analysis.

### 4. Results

#### 4.1. Wind velocities based on lidar data

The lidars deployed offer a suitable spatiotemporal resolution, allowing us to analyse the horizontal wind velocity field up to 5 kilometres from the instruments. An example of line-of-sight velocity captured by Donald and Dolly in a selected 1-hour interval can be seen in fig. 3.

Dolly records values between 1 m/s and -5 m/s along the lidar beam, while the Donald unit measures velocity components from -5 m/s to -11 m/s. Noticing the decreased wind speeds, Dolly observes a transformation in sign along the scanning line, while Donald's laser beam is more aligned with the main direction of the incoming wind. In the present campaign, the positive LOS velocity was adopted away from the lidar, opposite to a convention presented in fig. 2. The negative wind velocities in fig. 3 thus correspond to wind towards the lidar, from the north. Large gusts are observed in the entire monitored domain by both lidars during the first 12 minutes of

the 1-hour interval examined.

Beyond 3800 meters, Dolly is seen to produce noisy or missing data (white colour) when the beam strikes the hard target (mountains). Another portion of noisy data is seen at the end of the 1-hour interval in both lidar signals, which may be associated with a reduced amount of aerosols in the air being measured. This is also seen at ranges above 3000 m between 3:10 and 3:30, however, that does not affect the extraction of the 2D horizontal wind components by direct formulation, at the intersection points between the lidar beams from Donald and Mikke with the lidar beam from Dolly.

The direct formulation explained in section 3.1 was used to construct the wind direction and along wind velocity, as reference information for the flow conditions in the middle of the fjord. The intersection point between Donald and Dolly gave a mean along wind velocity of 9.67 m/s with an average orientation of 4.59° from North, while the intersection point between Mikke and Dolly gave 9.66 m/s and 4.97°.

*4.2. Mean wind direction based on PPI*
Figure 4 shows the averages of the LOS wind velocity derived from PPI scans measured by Minni over 1.5° wide azimuth sectors in the interval studied for the December 2020 event. A wind speed reduction is illustrated at the boundaries of the mountain, especially the mountains in Sula island. Some disturbances are seen in the sectors between 30° and 60° at the 3.4 km and 5.4 km range. These are associated with large values of CNR and high atmospheric backscatter coefficients coming from a hard target located in the northeast. The sector positioned at the angle of 156°, recorded on 1 December 2020, 03:00 to 04:00, has the highest LOS wind velocity. The largest positive wind speeds are for the wind direction away from the lidar, i.e. for the wind direction from 336° (NW) in a common meteorological reference system. This indicates that the wind entering the fjord from NE is accelerated through the fjord "channel" defined by the steep hills and then it adopts the fjord orientation, veering to a NW direction.

*4.3. Velocity based on parallel-positioned lidar beams*
Having only a 1.13° deviation between the laser beams of Donald and Mikke makes the beams close to parallel and the LOS wind velocities mapped by them nearly identical in terms of wind speed levels. This allows us to compare the regions of interest in the flow mapped by Donald and Mikke to analyse the shift in time and space of the flow pattern between the two observation lines. An example of a shift in flow pattern tested is indicated as the region of interest (ROI) by a red square in fig. 3 (top) for Donald and fig. 5 (top) for Mikke. The contents of the red square in both figures are magnified in the bottom panels of fig. 5. Applying an ECC algorithm [18] on the two ROIs shows that a shift of 6.83 units in time and 2.50 units in space for the image created for Mikke gives the highest correlation with the template image provided by Donald. These shifts are illustrated with red lines in the image for Mikke's ROI. It is worth noting, that the resolution in time is 1 second and in space is 25 meters.

By knowing the amount of movement in space between the template and the shifted images, it is possible to compute the wind direction by comparing the ranges of the two lidars as illustrated in fig. 6, by the purple arrow assuming that the turbulence is frozen between the two beams. Using this analogy, the "instantaneous" wind direction is derived to be equal to 353.5°. Since the defined ROI includes the intersection between Donald and Mikke, the derived wind direction can be compared to the one calculated at the intersection point by the direct formulation explained in 3.1. For the duration of 185 s for which the ROI is defined, the mean wind direction at the intersecting point is calculated equal to 356.5° which is close to the value derived by the image processing approach i.e. ECC algorithm.

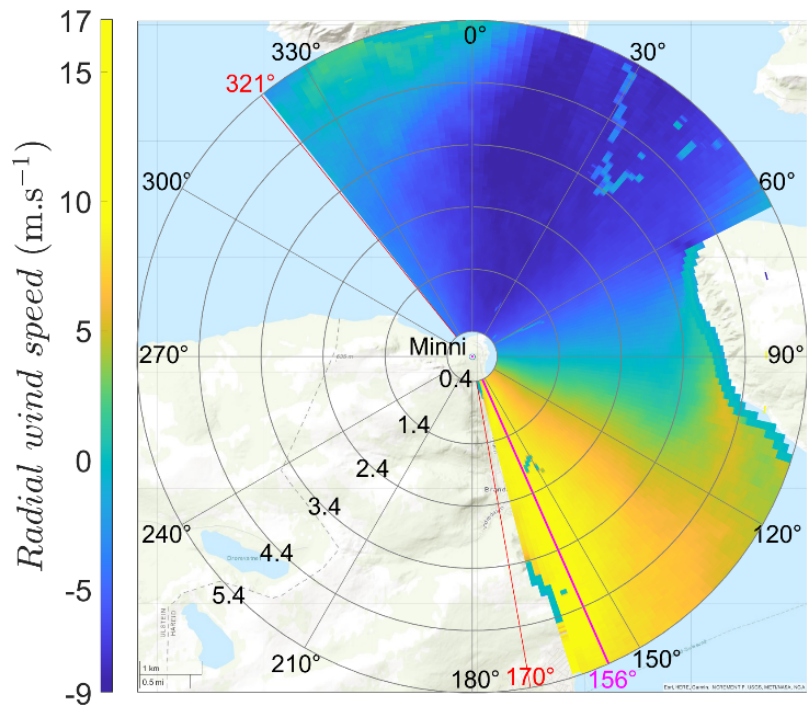The lidar measures the along beam wind speed which has a relation with the main wind speed

**Figure 4.** Mean of the along-beam wind velocity derived from PPI scans recorded on 1 December 2020, 03:00 to 04:00. Positive velocity is away from the lidar.
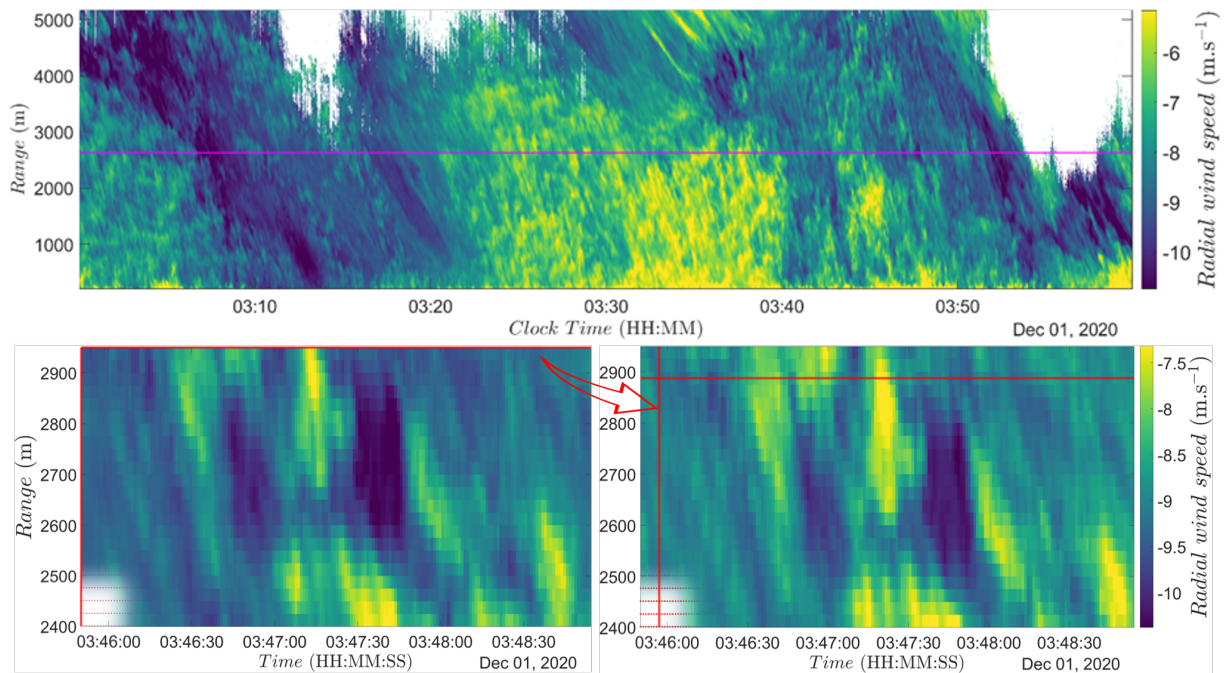


**Figure 5.** (top) Spatiotemporal fluctuations of wind velocity recorded on 1 December 2020, 03:00 to 04:00 by Mikke. Region of interest within the data from Donald (bottom-left) and Mikke (bottom-right). The red arrow indicates the time and distance shift in the flow pattern between the two lidar beams.
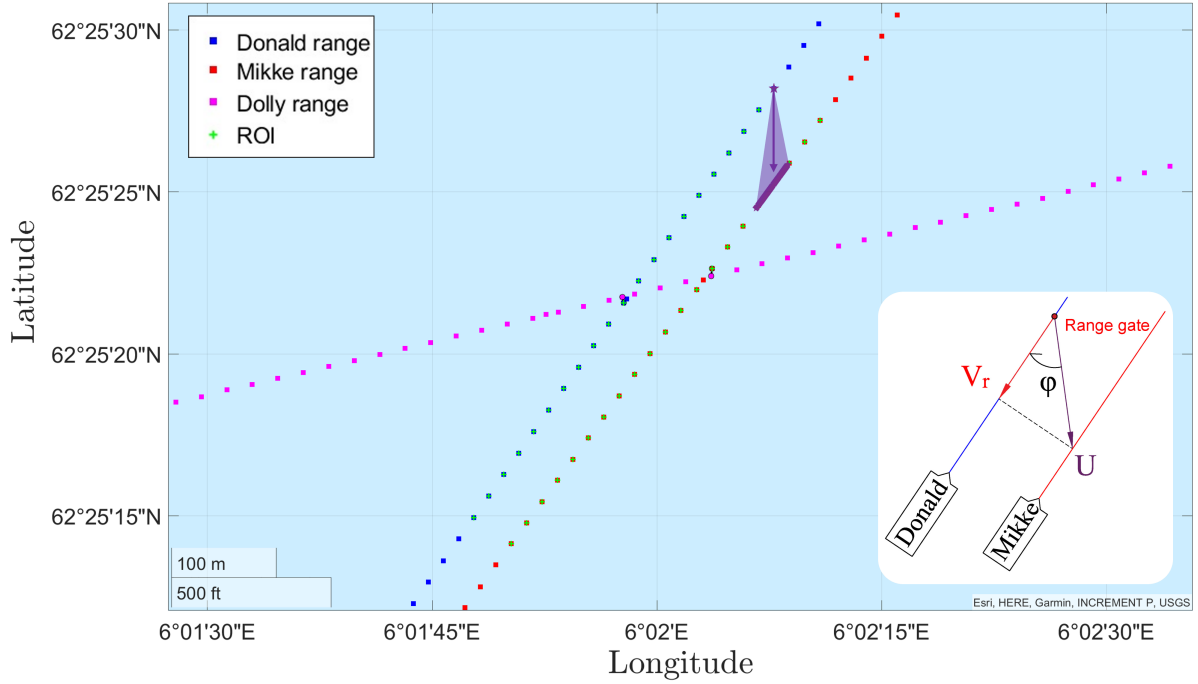
**Figure 6.** Plan view of the measurement domain of lidars for LOS mode in the middle of the fjord.

as

$$V_r(t) = U(t).\cos(\phi(t)) \tag{8}$$

where $U(t)$ is the along wind speed, and $\phi(t)$ is the angle between the along wind speed and beam orientation, computed by the ECC algorithm as illustrated in fig. 6. Once $V_r$ and $\phi$ are known, the along wind speed can be easily obtained through Eq. (5). The algorithm has been applied to a strip with a length of 500 meters for the flow mapped by both Donald and Mikke, as indicated by green markers in fig. 6. The purple triangle in fig. 6 shows an envelope of computed $\phi(t)$ in the selected 1-hour interval.

Since the intersection point is embedded in the ROI, a comparison between the time series of wind direction and wind speed can be made between results from the image processing approach and the direct formulation. This is done in fig. 7, where the time series derived by the image processing approach is shown and compared with the time series based on the direct formulation for the intersection point of Donald and Dolly.

Due to the predefined resolution in space between observation points (25 m), the variation of the wind direction captured by the image processing approach is smoothened, compared to the time series at the intersection point, but is still a good estimate of the wind direction in the region being studied. The image processing approach is further seen to accurately reconstruct the wind velocity derived at the intersection point.

The correlation plot of the along wind velocity, $U$, computed by the two approaches is shown in fig. 8. Although some scattering is visible in the reconstructed wind speed, the regression line resembles $x = y$ quite well and yields a reasonable goodness-of-fit coefficient of $R^2 = 0.903$ for the period considered.
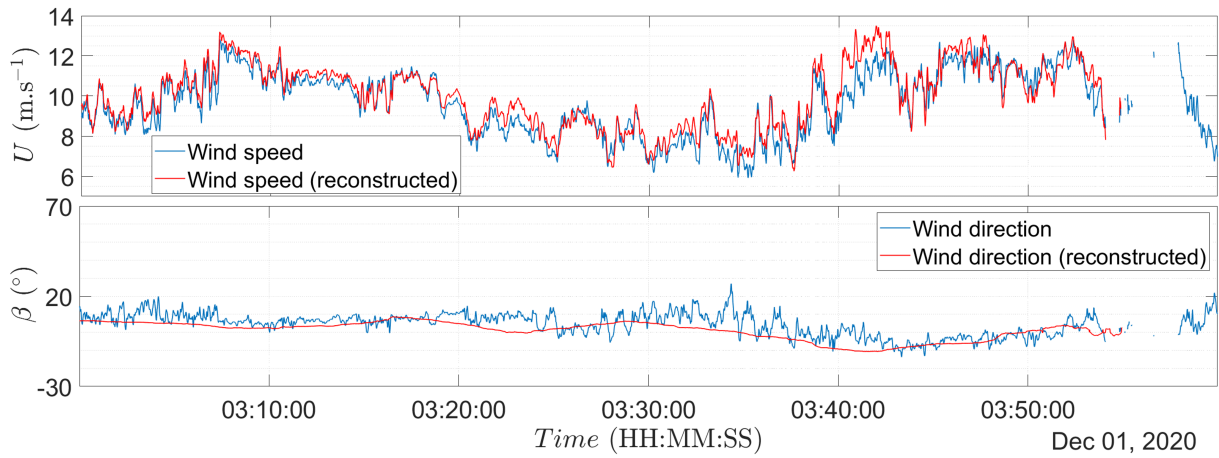
**Figure 7.** Time-series of the mean wind speed ($U(t)$) and wind direction ($\beta$) in the intersection point of Donald and Dolly on 1 December 2020, 03:00 to 04:00.
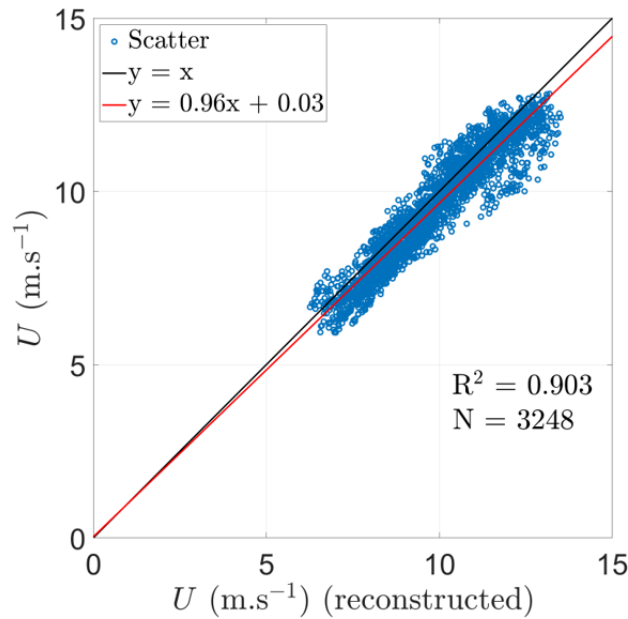


**Figure 8.** Correlation of the mean wind speed ($U$) recorded on 1 December 2020, 03:00 to 04:00.

## 5. Conclusions and Further Works

A system of 2 pairs of long-range lidars was deployed at Sulafjorden in Norway to monitor the horizontal wind field and record wind data to provide a design base for a planned fjord-crossing. One of the lidars was set to operate in PPI scanning mode while three others worked in LOS mode providing two intersection points in the middle of the fjord. The long-range lidar system was able to capture the wind in the fjord, and large gusts within the monitored domain were seen to be captured by all the lidars.

Measurements in PPI mode reveal that the wind entering the fjord from NE is accelerated through the fjord "channel" defined by the steep hills on either side, and that the flow then follows the fjord orientation, veering to an NW direction.

In order to resolve the wind speed and direction in an extended domain around the planned bridge span, the Enhanced Correlation Coefficient Maximization technique was used to evaluate

the along wind speed based on image mapping of data from two nearly-parallel lidar beams. A resulting time series from a location close to an intersecting lidar beam was then compared to results provided by a direct approach based on the intersecting LOS velocities. The image-based analysis using the ECC technique showed reasonable performance with a goodness-of-fit coefficient of $R^2 = 0.903$ for the evaluation of the along wind speed. The wind direction estimates are also accurate in the mean, but due to the limited spatiotemporal resolution of the lidar LOS data, the natural fluctuations are somewhat smoothed.

The image processing approach introduced, provides an opportunity to evaluate the wind direction and wind velocity at any range gate observed for the two nearly parallel lidar beams. The approach may however be sensitive to the distance between the two parallel beams and more events need to be studied to evaluate the accuracy of the introduced image processing approach. An improved spatiotemporal resolution of the flow mapped by lidars would enable the estimation of more realistic fluctuations in the wind direction.

### References

[1] Nafisifard M, Jakobsen J B, Cheynet E, Snæbjörnsson J, Sjöholm M and Mikkelsen T 2021 *IOP Conf. Ser.: Mater. Sci. Eng.* vol 1201 (IOP Publishing) p 012008

[2] Nafisifard M, Jakobsen J B, Snæbjörnsson J, Sjöholm M and Mann J 2023 *J. Wind Eng. Ind. Aerodyn.* **240** 105491

[3] Nafisifard M, Jakobsen J B, Snæbjörnsson J, Sjöholm M and Mann J p (Accepted for publication)

[4] Cheynet E, Jakobsen J B, Snæbjörnsson J, Reuder J, Kumer V and Svardal B 2017 *J. Wind Eng. Ind. Aerodyn.* **161** 17–26

[5] Cheynet E, Jakobsen J B, Snæbjörnsson J, Mann J, Courtney M, Lea G and Svardal B 2017 *Remote Sens.* **9** 1–26

[6] Cheynet E, Jakobsen J B, Sverdal B, Reuder J and Kumer V 2016 *Energy Procedia* 462–477

[7] IEC61400-1 2005 *IEC 61400-1 Wind turbines, Part 1: Design requirements* (Norwegian electrotechnical publication)

[8] Andersen O J and Løvseth J 2006 *Mar. struct.* **19** 173–192

[9] Analysis: Lessons learned from wind lidar measurement campaigns for wind farms, bridges and airports during 2017-2021 https://www.vindteknikk.com/news/analysis-lessons-learned-from-wind-lidar-measurement-campaigns-for-wind-farms-bridges-and-airports-during-2017-2021/ kjeller Vindteknikk, 26 October 2021

[10] Ágústsson H 2022 E39, sulafjorden, møre & romsdal, analysis of lidar derived wind measurements, rap-kvt-lid-110-r1 / kvt/2021/r093/hÁ rev1 Tech. rep. Kjeller Vindteknikk, Norconsult (limited access)

[11] Furevik B R, Ágústsson H, Borg A L, Midjiyawa Z, Nyhammer F and Gausen M 2020 *Earth Syst. Sci. Data* **12** 3621–3640

[12] The Norwegian Public Roads Administration presented preliminary projects for possible bridge concepts for the sulafjorden https://www.vegvesen.no/vegprosjekter/europaveg/e39sulafjorden/nyhetsarkiv/statens-vegvesen-presenterte-forprosjekter-for-mulige-brukonsepter-for-sulafjorden/ statens Vegvesen, 10 June 2022

[13] Evangelidis G D and Psarakis E Z 2008 *IEEE Trans. Pattern Anal. Mach. Intell.* **30** 1858–1865

[14] Chizari A, Schaap M J, Knop T, Boink Y E, Seyger M M B and Steenbergen W 2021 *Sci. Rep.*

[15] Boquet M, Royer P, Cariou J P and Machta M 2016 *J. Atmos. Oceanic Technol.* **33** 977–987

[16] Alismail H 2016 *Direct Pose Estimation and Refinement (PhD thesis)* Ph.D. thesis Carnegie Mellon University Pittsburgh

[17] Kumar V M, Reuder J and Furevik B R 2014 *Energy Procedia* 214–220

[18] ECC image alignment algorithm (image registration) https://www.mathworks.com/matlabcentral/fileexchange/27253-ecc-image-alignment-algorithm-image-registration georgios Evangelidis, 4 October 2023